



Response of Earth's magnetic field to large lower mantle heterogeneity

Swarandeeep Sahoo^a, Binod Sreenivasan^{b,*}

^a Department of Applied Geophysics, Indian Institute of Technology (ISM), Dhanbad 826004, India

^b Centre for Earth Sciences, Indian Institute of Science, Bangalore 560012, India

ARTICLE INFO

Article history:

Received 11 February 2020

Received in revised form 18 July 2020

Accepted 27 July 2020

Available online xxx

Editor: M. Ishii

Keywords:

geomagnetic field

core flows

core–mantle interaction

ABSTRACT

A simplified two-fold pattern of convection in the Earth's core is often used to explain the non-axisymmetric magnetic flux concentrations in the present day geomagnetic field. For large lateral variations in the lower mantle heat flux, however, a substantial east–west dichotomy in core convection may be expected. This study examines the effect of a large lateral variation in heat flux at the outer boundary in cylindrical annulus experiments that achieve approximate geostrophy of the convection as well as in rapidly rotating spherical shell simulations. In either geometry, the imposed boundary heat flux is derived from the seismic shear wave velocity in the lowermost mantle. The pattern of large-scale convection in the simulations closely follows that in the annulus experiments, which suggests that the lateral buoyancy at the equator essentially determines the structure of core convection. In particular, the location of a coherent downwelling that forms beneath Canada in mildly driven convection entirely switches over to the Siberian region in strongly driven states. Spherical dynamo models in turn show that this eastward migration of convection causes the relative instability or even the disappearance of the high-latitude magnetic flux in the Western hemisphere. Finally, large radial buoyancy causes homogenization of convection, which may place an upper bound for the Rayleigh number in the core.

© 2020 Elsevier B.V. All rights reserved.

1. Introduction

Observation of the Earth's magnetic field has shown flux concentrations at the core–mantle boundary (CMB) that are symmetric about the equator near regions of high seismic shear wave velocity in the lower mantle. This led to the argument that relatively cool regions of the lower mantle, where persistent subduction took place over tens of millions of years (Van der Hilst et al., 1997; Grand, 2002), would preferentially extract heat from the core, causing enhanced convection and magnetic flux generation beneath the CMB (Bloxham and Gubbins, 1987; Gubbins and Kelly, 1993; Hoffman et al., 2008; Olson, 2016). Spherical shell dynamo models have explored this idea by imposing a spatially varying temperature or heat flux at the outer boundary (Olson and Christensen, 2002; Gubbins et al., 2007; Olson et al., 2015) that is linearly correlated to a tomographic model of the seismic shear wave velocity in the lowermost mantle (Masters et al., 1996).

Although the largest term in the spherical harmonic expansion of the shear wave velocity is Y_2^2 , the 4 main lobes in the Earth's field have shown deviations from the simple two-fold longitudinal variation. The “Canadian” pair of lobes in the West have been his-

torically more mobile than the “Siberian” pair in the East, and the Canadian flux patch split in two in the mid-19th century (Jackson et al., 2000; Gubbins et al., 2007; Amit et al., 2011). A marked eastward drift of Earth's magnetic North, from Canada towards Siberia (Olsen and Mandea, 2007), is consistent with an inhomogeneous core flow regime that produces highly time-varying magnetic flux in the West and relatively stable magnetic flux in the East. If the inhomogeneity induced by the mantle should in addition contribute to the seismic anisotropy of the inner core (Bergman, 1997; Aubert et al., 2008; Gubbins et al., 2011), a substantial east–west dichotomy in core convection should be expected. Given that the shear wave anomaly beneath America is stronger than that beneath Asia, one would anticipate, based on current understanding, that a coherent downwelling beneath the seismically faster region should concentrate stable magnetic flux beneath Canada. This is contrary to observation, where the Siberian magnetic flux is more stable. The aim of this paper is to identify a core flow regime that would adequately support the observed field variation.

Since the heat flux variation on the Earth's CMB is predominantly symmetric about the equator (e.g. Masters et al., 2000), we hypothesize that the azimuthal variation of the equatorial heat flux would control the structure of convection in the core. Consequently, a simplified experimental model is considered wherein convection in a rotating cylindrical annulus is subject to purely azimuthal variations in outer boundary heat flux. Convection in the

* Corresponding author.

E-mail address: bsreeni@iisc.ac.in (B. Sreenivasan).

core is modelled in the experiment by using centrifugal acceleration as gravity and a radial temperature gradient that is reversed in direction (see Busse and Carrigan, 1974, 1976). The columnar fluid motion that occurs in rapidly rotating convection was noted in laboratory experiments of convective onset in cylindrical annuli (Busse and Carrigan, 1974) and spherical shells (Busse and Carrigan, 1976; Carrigan and Busse, 1983; Hart et al., 1986). Supercritical convection experiments (Cardin and Olson, 1994; Aubert et al., 2001) and simulations (Aurnou et al., 2015) indicated that the columnar flow is largely preserved in strongly driven rotating systems. Experiments on rotating convection in a hemispherical shell with a localized boundary heat source (Sumita and Olson, 1999, 2002) showed a jet-like downwelling originating from the heat flux anomaly. The response of rotating convection to a large-scale two-fold variation in outer boundary heat flux was examined recently (Sahoo and Sreenivasan, 2019) by imposing equally enhanced heat fluxes relative to the mean heat flux in diametrically opposite sectors of a cylindrical annulus. The present experiment, on the other hand, examines the effect of imposing boundary heat fluxes of different magnitudes in the sectors representing the Canadian and Siberian regions, in line with the tomographic model of shear wave velocity (Masters et al., 1996, 2000). In this model, the dominant variation is that of the wavenumber $m = 2$, the magnitude of which is nearly twice that of $m = 1$. That said, the threshold for convective onset is lower for the $m = 1$ component than for $m = 2$ (Sahoo and Sreenivasan, 2017). Therefore, an east–west dichotomy in the pattern of convection would likely result from a large azimuthal variation in outer boundary heat flux.

An advantage of using a cylindrical annulus rather than a spherical annulus in the laboratory simulation of core convection is that the approximate axial invariance of the z vorticity (quasi-geostrophy) is realized even with large azimuthal variations in boundary heat flux (Sahoo and Sreenivasan, 2019). The quasi-geostrophic constraint is considered important in core flow modelling since a large thermal heterogeneity at the boundary inhibits dynamo action in rotating spherical shells (Olson and Christensen, 2002; Takahashi et al., 2008; Sreenivasan, 2009), probably due to the breakdown of columnar convection. The obvious drawback of using a cylindrical annulus is that the generation of thermal Rossby waves (Azouni et al., 1985; Zhang and Gubbins, 1996) and the rotational dependence of the flow length scale (Carrigan and Busse, 1983) that follows from linear theory of onset (e.g. Dormy et al., 2004) are suppressed. By comparing the flows obtained in the cylindrical annulus experiments and spherical shell simulations, we aim to show that the absence of these flow properties does not limit our understanding of the structure of convection in a strongly driven regime. Rather, the interaction between the lateral heterogeneity and gravity at the equator largely determines the organization of core convection.

2. Methods: laboratory experiments and numerical simulations

In this section, we first present the details of the laboratory experiment used to study thermal core–mantle interaction. Second, the computational model used for the hydrodynamic and magnetohydrodynamic (MHD) simulations is described. Finally, a comparison is presented of the patterns of lateral heterogeneity used in the experiments and computations.

2.1. The laboratory experiment

The experiments consist of purely thermal convection in water in a rapidly rotating cylindrical annulus with an imposed azimuthal variation in outer boundary heat flux. The right circular annular gap, measuring 370 mm in height with inner and outer radii $r_i = 50$ mm and $r_o = 142$ mm respectively, is filled with water

and rotated at the rate of 300 revolutions per minute. A schematic of the assembled set-up is shown in Fig. 1. The inner cylinder is made of aluminium while the outer cylinder is made from polymethyl methacrylate (PMMA). The top and bottom ends are sealed using flat PMMA discs of width 50 mm. The transparent PMMA enables the illumination of a horizontal plane by an array of lasers and quantitative measurements of velocity in the experiments via particle image velocimetry (PIV). A detailed description of the instrumentation and data logging is given in a recent paper (Sahoo and Sreenivasan, 2019).

The inner cylinder is maintained at a temperature of $T_i = 22 \pm 0.1$ °C by the circulation of water from a constant-temperature bath. At the outer cylinder, a constant heat flux is generated by a heating element made of 0.4 mm Ni-Cr wires. The thick top and bottom plates act as insulating surfaces, enabling predominantly radial heat transport from the outer cylinder to the inner cylinder.

For a fixed angular speed Ω of 300 revolutions per minute, the rotational Froude number $Fr = \Omega^2 L/g$ is 9.26 and the Ekman number $E = \nu/2\Omega L^2$ is 1.8×10^{-6} , where L is the annulus width, g is the gravitational acceleration and ν is the kinematic viscosity of water at 298 K. Because rotation is rapid enough to yield approximate geostrophy of the convection (Sahoo and Sreenivasan, 2019), the precise value of E in the experiment is immaterial. The Rayleigh number, $Ra = \Omega^2 \alpha \beta L^5 / \nu \kappa$ is varied in the approximate range $1 \times 10^8 - 6 \times 10^9$ (Table 1), spanning near-critical to strongly supercritical regimes. Here, α is the thermal expansion coefficient, β is the temperature gradient at the outer boundary and κ is the thermal diffusivity. The Prandtl number, $Pr = \nu/\kappa$ of water is 6.64.

2.2. Computational model

We consider a rotating convection-driven dynamo operating in an electrically conducting fluid confined between two concentric, corotating spherical surfaces that correspond to the inner core boundary (ICB) and the core–mantle boundary (CMB). The ratio of inner to outer radius is chosen to be 0.35. Lengths are scaled by the thickness of the spherical shell L , and time is scaled by the magnetic diffusion time, L^2/η , where η is the magnetic diffusivity. The velocity field \mathbf{u} is scaled by η/L , the magnetic field \mathbf{B} is scaled by $(2\Omega \rho \mu \eta)^{1/2}$ where Ω is the rotation rate, ρ is the fluid density and μ is the magnetic permeability. The scaled magnetic field (Elsasser number Λ) is an output derived from our dynamo simulations as a root mean square (rms) value, where the mean is a volume average. The non-dimensional MHD equations solved in the model are given in Supplementary Material.

In the simulations, the Ekman number E has the same definition as in the experiments. The Rayleigh number is defined by $Ra = g \alpha \beta L^4 / \nu \kappa$, where g is the gravity acting radially inward. The Prandtl number $Pr = \nu/\kappa$ and the magnetic Prandtl number $Pm = \nu/\eta$ give the ratio of viscous to thermal and viscous to magnetic diffusivities respectively. The basic state non-dimensional temperature profile represents a conventional basal heating, $T_b(r) = \beta/r$. We set an isothermal condition at the ICB and a constant heat flux condition at the CMB. The velocity and magnetic fields satisfy the no-slip and electrically insulating conditions respectively. The fixed parameters used in the simulations are $E = 2 \times 10^{-6}$ and $Pr = Pm = 1$. For each dynamo calculation in Table 2, a non-magnetic calculation is done at the same parameters to enable comparison with laboratory convection. The calculations are performed by a code that uses spherical harmonic expansions in the angular coordinates (θ, ϕ) and finite differences in radius r (Willis et al., 2007).

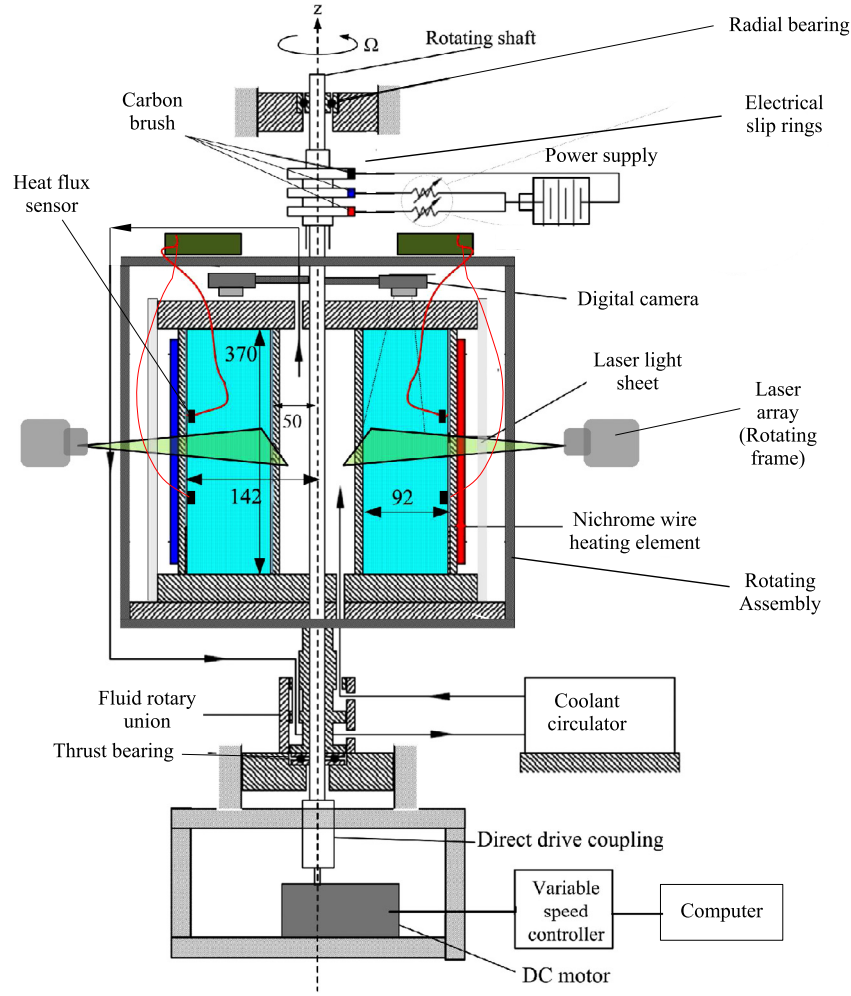


Fig. 1. The schematic of the experimental set-up used to study rotating convection in an annulus with azimuthally varying outer boundary heat flux.

Table 1

Summary of the experimental runs showing the input voltage to the heating element at the outer boundary, Ra is the Rayleigh number defined above (section 2.1), Q_w is the measured boundary heat flux in the “Western” sector ($30^\circ W < \phi < 120^\circ W$ in Fig. 2(b)), Q_e is the measured heat flux in the “Eastern” sector ($70^\circ E < \phi < 120^\circ E$) and Q_m is the mean boundary heat flux. The dimensionless measure of boundary heat flux heterogeneity, $q^* \approx 2.4$ in all the runs. The local buoyancy parameter R^* , defined by (2), is given separately for the Western (W) and Eastern (E) halves of the annulus. The local onset Rayleigh numbers $Ra_{c,e}$ are $\approx 1.517 \times 10^8$ (W) and $\approx 2.852 \times 10^8$ (E) respectively. The superscript † indicates the occurrence of a coherent downwelling in either half of the annulus.

Voltage (V)	Ra ($\times 10^8$)	Ra/Ra_c	Q_w (Wm^{-2})	Q_e (Wm^{-2})	Q_m (Wm^{-2})	Ra_W ($\times 10^8$)	Ra_E ($\times 10^8$)	R^*_W	R^*_E
20	1.22	0.96	13.88	9.38	5.82	1.45	0.98	0.96	0.34
25	1.27	1.00	14.52	9.82	6.09	1.52	1.03	1.00	0.36
30	1.35	1.06	15.37	10.49	6.47	1.61	1.10	1.06	0.38
60	3.52	2.76	40.03	27.29	16.83	4.18	2.85	2.76†	1.00
90	8.92	7.01	102.54	68.24	42.7	10.70	7.13	7.06†	2.50
120	17.7	13.89	202.14	136.18	84.58	21.1	14.2	13.9	4.98†
150	36.0	28.3	410.25	278.89	172.29	42.9	29.1	28.3	10.22†
180	60.6	47.6	692.34	466.58	289.73	72.3	48.8	47.7	17.10

2.3. Lateral heterogeneity in the experiments and computations

The pattern of heat flux imposed at the outer boundary is derived from the laterally inhomogeneous density at the core–mantle interface related to the seismic shear wave velocity variation (Masters et al., 2000). Fig. 2(a) shows the map of shear wave velocity anomaly at the CMB (Willis et al., 2007) which is assumed to be directly proportional to the heat flux anomaly. In the computations, the dimensionless measure of the boundary heterogeneity is

$$q^* = \frac{\text{Maximum flux variation}}{\text{Mean flux}} = 4, \quad (1)$$

which, on the equator, gives extremum fluxes of 3.32 (America), -0.573 (Africa), 2.317 (Asia) and -1.928 (Pacific). The negative values above represent heat flow into the core from the mantle, which give a stably stratified basic state beneath the CMB. In the experiments, the equatorial variation in heat flux is approximated by dividing the heating element on the outer cylinder into four nearly equal-area sectors. Different electric currents are passed through each sector via rheostats, producing an azimuthally varying heat flux as in Fig. 2(b).

Fig. 2(c) shows a comparison of the total “tomographic” heat flux at the CMB equator (black line) with the flux entering the an-

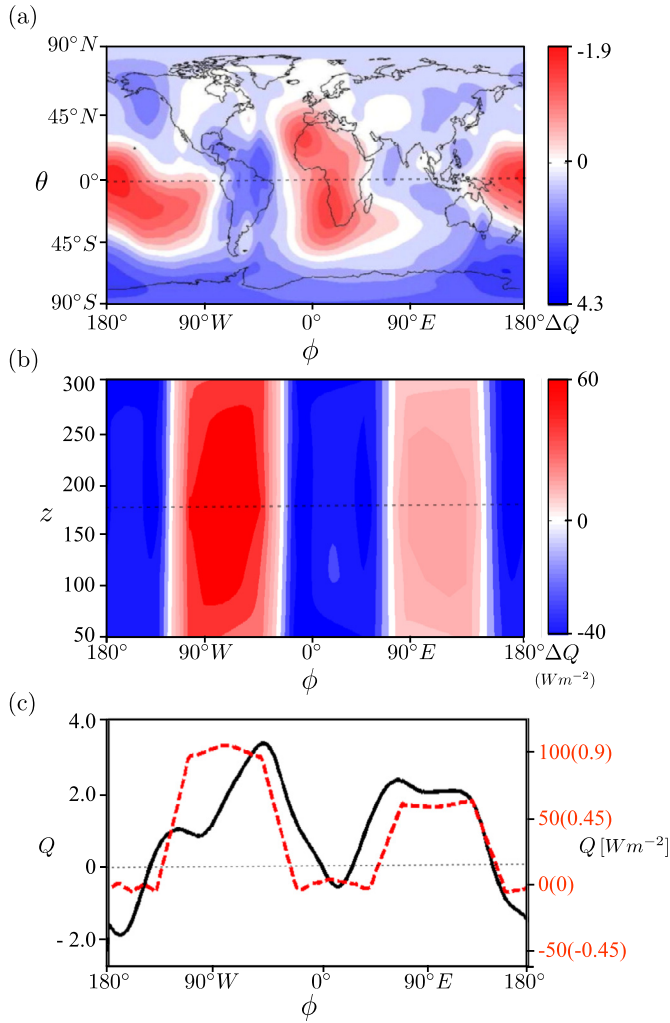


Fig. 2. (a) Pattern of the heat flux variation (ΔQ) on the outer boundary of the spherical shell model derived from the seismic shear wave velocity at the base of the mantle (e.g. Willis et al., 2007). (b) Heat flux variation (relative to the mean value) measured on the outer cylinder of the annulus in an experimental run with $Ra = 8.92 \times 10^8$ and $q^* \approx 2.4$. (c) Comparison of the azimuthal variation of the measured outer boundary heat flux in the experiment (red dashed line) with the respective tomographic value (black line) at the equator in the spherical shell model. The experimental values are also shown in dimensionless units within brackets. The heat flux is scaled by $\Delta T/L = 113 Wm^{-2}$, where ΔT is the basic state temperature difference between the inner and outer surfaces of the annulus. In the experiment, heat enters through the outer boundary, whereas in the simulation, heat escapes through it. (For interpretation of the colours in the figure(s), the reader is referred to the web version of this article.)

nulus at the mid-height of the outer cylinder (red dashed line). In the annulus model, the $m = 2$ variation in the boundary heat flux is approximately twice that of $m = 1$, as in the tomographic condition. The peak heat fluxes below South America and East Asia are well reproduced in the experiment. (There is, however, a longitudinal misalignment of 30° in the location of the peak below America due to the east–west asymmetry of the tomographic heat flux.) The ratio of the measured heat fluxes in the “Western” ($30^\circ W < \phi < 120^\circ W$) to the “Eastern” ($70^\circ E < \phi < 120^\circ E$) sectors of the experiment, Q_w/Q_e (Table 1) is kept equal to the ratio of the peak equatorial fluxes in the American to the Asian regions. However, the inward heat fluxes beneath Africa and the Pacific are not reproduced, for the experiment has nearly zero heat flux in the corresponding sectors. The assumption here – that the basic state thermal stratification in these regions would not produce a first-order change in the convection pattern – is eventually borne

out by our spherical shell simulations. The resulting value of q^* in the experiment, $(Q_w - 0)/Q_m \approx 2.4$, where Q_m is the mean outer boundary heat flux (Table 1). While the African and Pacific sectors in the experiment are neutrally stable, the east–west asymmetry in the heat fluxes yields a value of $q^* > 2$.

3. Results

3.1. Convection experiments in a cylindrical annulus

Fig. 3 shows the patterns of convection in the experiment at $q^* = 2.4$ and progressively increasing Rayleigh number Ra starting from the onset of convection to ≈ 48 times the onset value, Ra_c . The plots are averaged over 360 s, needed to ensure reproducibility of the flows over multiple experiments. This period is ~ 20 times the turnover time scale, estimated from the ratio of the length scale (0.092 m) to the characteristic velocity ($\sim 5 \times 10^{-3} ms^{-1}$). This averaging time ensures the visualization of coherent (long-lived) flow structures that are not otherwise visible in snapshots. The convection in Fig. 3 is approximately geostrophic due to the purely azimuthal variation of the imposed boundary heat flux (Sahoo and Sreenivasan, 2019). Fig. 3(a) shows the onset of convection in the experiment subject to the Earth-like pattern of the boundary heat flux variation in Fig. 2(b). The onset occurs close to the outer boundary where the viscosity is the smallest (Sahoo and Sreenivasan, 2019; Ahlers et al., 2006). At $Ra = 1.27 \times 10^8$, convection sets in preferentially in the Western sector $30^\circ W < \phi < 120^\circ W$ (spanning America) where the outer boundary heat flux is largest, whereas the Eastern sector $70^\circ E < \phi < 120^\circ E$ (spanning Asia) with relatively lower boundary heat flux is quiescent. By contrast, the simple two-fold pattern of heat flux, wherein the fluxes in diametrically opposite sectors are equal, would have produced convection of equal intensity in the two sectors where the heat flux is equally enhanced relative to the mean (see Sahoo and Sreenivasan, 2019). We anticipate that this difference in the convection pattern between the two-fold and Earth-like patterns would persist with progressively stronger thermal forcing, examined further in Fig. 3(b)–(f). The Western sector goes through a series of convection patterns at progressively increasing Ra ; similar patterns occur in the Eastern sector over a range of higher Ra values. For $Ra \approx 3 \times 10^8 - 9 \times 10^8$ (Fig. 3(b) & (c)), convection beneath Canada takes the form of a dominant downwelling sandwiched between a coherent cyclone–anticyclone vortex pair, whereas convection beneath Asia sets in and then forms a cluster of small-scale vortices. For $Ra \approx 1.7 \times 10^9 - 4 \times 10^9$, a coherent vortex pair forms beneath Asia, whereas the vortex pair beneath Canada breaks down into small-scale clustered convection due to the large boundary heat flux in that sector (Fig. 3(d) & (e)). The switch in the site of the coherent downwelling is analysed by defining a local buoyancy parameter,

$$R^* = \frac{Ra_\ell}{Ra_{c,\ell}}, \quad (2)$$

where Ra_ℓ is the Rayleigh number based on the mean boundary heat flux in either half of the annulus and $Ra_{c,\ell}$ is the critical (onset) value of the local Rayleigh number. The values of R^* at which a coherent downwelling occurs in the East and West, denoted by the superscript \dagger in Table 1, are comparable. Notably, Fig. 3(c) suggests that a coherent downwelling in the Eastern hemisphere is close to developing as might be expected for the value of $R^*_E = 2.5$, compared with the value of $R^*_W = 2.76$ at which a coherent downwelling is clearly visible in the West. Furthermore, the loss of this coherent structure between $R^*_W = 7.07$ and 13.9 is

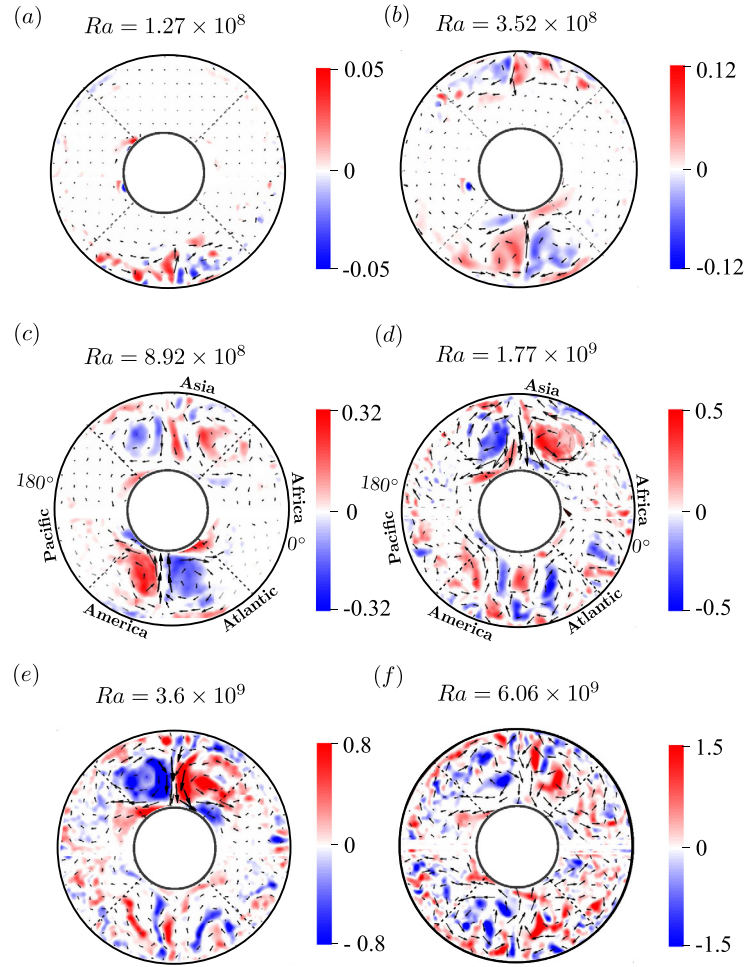


Fig. 3. The measured horizontal velocity vectors (arrows) superposed on shaded contours of the z -vorticity (s^{-1}) on a horizontal (r, ϕ) plane at height $z = 180$ mm of the experimental annulus. The Earth-like pattern of CMB heat flux anomaly, approximated by Fig. 2(b), is imposed on the outer boundary. The Rayleigh number Ra is progressively increased for a fixed boundary heterogeneity $q^* = 2.4$. The dotted lines separate the four nearly equal-area sectors.

consistent with its presence at $R_E^* = 10.22$. In short, as Ra is progressively increased, the Western and Eastern halves pass through a similar range of R^* in succession.

The remarkable switch of the coherent downwelling from the Canadian to the Siberian region occurs despite the fact that the heat flux anomaly is largest beneath the Canadian region. One would therefore expect a coherent magnetic flux concentration beneath Siberia and a relatively unstable flux beneath Canada, provided Ra is large and q^* is not small. As Ra is increased further to $\sim 6 \times 10^9$ (Fig. 3(f)), convection beneath Siberia also breaks down into small scales, at which point convection spills over into the African and Pacific regions represented in the experiment to produce a nearly homogenized state. The experimental runs in the range of $1.7 \times 10^9 < Ra < 4 \times 10^9$ therefore seem to lie in the ‘sweet spot’ for Earth-like behaviour, likely resulting in a mobile Canadian pair and a quasi-stationary Siberian pair of high-latitude magnetic flux lobes.

The patterns of convection that emerged from Fig. 3 are further evident in Fig. 4, where the radial velocity is shown across Ra . The isolated downwelling that forms in the Western sector at $Ra \approx 8.9 \times 10^8$ breaks into a cluster at higher Ra , whereas the isolated downwelling that appears in the Eastern sector at $Ra \approx 1.7 \times 10^9$ persists until convection homogenizes in the annulus. It must be emphasized that this strong east–west dichotomy in supercritical convection has its origins in the onset of convection itself, where the Western sector of higher boundary heat flux admits onset at a lower Ra than the Eastern sector. It is there-

fore reasonable to expect this phenomenon to occur in spherical shell convection, provided the east–west hemispherical dichotomy of the convection is preserved by the approximate geostrophy of the columnar flow.

3.2. Spherical shell convection simulations

In spherical shell convection with large q^* , the latitudinal variation in boundary heat flux would produce strong thermal winds (Sreenivasan, 2009) that cause loss of geostrophy. This should be countered by rapid rotation in the model, via a low Ekman number. To simulate this regime, we choose $E = 2 \times 10^{-6}$ with $q^* = 4$, which produces stable stratification beneath Africa and the Pacific. While the experiment has zero boundary heat flux in these regions, the numerical simulations provide the opportunity to examine the regime where the heat flux is reversed. Because the pattern of convection is now known to be determined by its onset, we look at the critical Rayleigh number Ra_c for convection to set in. Although Ra_c falls steeply relative to its value for homogeneous convection for $q^* \lesssim 1$ (see Sahoo and Sreenivasan, 2017, 2019), its value does not change significantly for $q^* > 2$ (Sahoo and Sreenivasan, 2017). For $q^* = 2.4 - 4$, Ra_c decreases only marginally from 6.2×10^6 to 6.05×10^6 . (E.g. $Ra_c = 6.12 \times 10^6$ for $q^* = 3$, and $Ra_c = 6.08 \times 10^6$ for $q^* = 3.5$.) This suggests that the structure of convection may not change appreciably due to the stably stratified regions beneath the outer boundary. We find below that this is indeed the case.

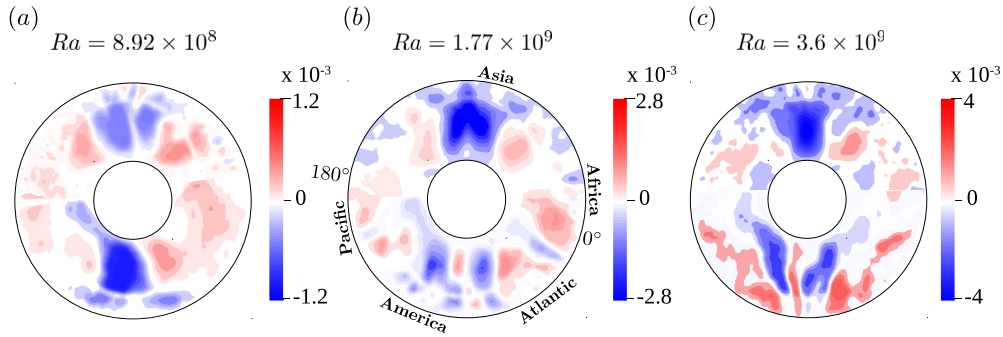


Fig. 4. Sectional ($z = 180$ mm) contour plots of the radial velocity (ms^{-1}) in the experiments at the indicated Rayleigh numbers.

Table 2

Summary of the pure convection and dynamo simulations considered in this study. Here, Ra is the Rayleigh number, l_{max} is the maximum spherical harmonic degree, N_r is the number of radial grid points, Re is the hydrodynamic Reynolds number, Rm is the magnetic Reynolds number and Λ is the Elsasser number given by the volume-averaged magnetic field strength. The simulations are performed at Ekman number $E = 2 \times 10^{-6}$, Prandtl number $Pr = 1$ and boundary heat flux heterogeneity $q^* = 4$. The local buoyancy parameter R^* , defined by (2), is given separately for the Western (W) and Eastern (E) hemispheres. The local onset Rayleigh numbers $Ra_{c,\ell}$ are $\approx 7.01 \times 10^6$ (W) and $\approx 2.79 \times 10^7$ (E) respectively. The superscript † indicates the occurrence of a coherent downwelling in either hemisphere.

Ra ($\times 10^8$)	Ra/Ra_c	l_{max}	N_r	Re	Rm	Λ	Ra_W ($\times 10^8$)	Ra_E ($\times 10^8$)	R_W^*	R_E^*
0.0605	1.0	128	120	≈ 0	–	–	0.0636	0.0582	0.9	0.2
1.0	16.5	200	180	225	169.6	1.11	1.05	0.96	15.0†	3.4
3.0	50	240	220	425	231.1	1.69	3.15	2.89	45.0†	10.3
8.0	132	240	220	828	370.1	2.46	8.41	7.70	120.0†	27.6
11.5	190	240	220	947	436.4	2.82	12.1	11.1	172.5	39.6†
15	248	240	220	1037	468.2	3.10	15.8	14.4	225.0	51.7†
25	413	256	220	1419	629.2	3.66	26.3	24.0	374.9	86.2†
60	992	384	360	4682	–	–	63.1	57.7	900.0	206.9

The numerical simulations of spherical shell convection are performed at $Pr = 1$ and progressively increasing Rayleigh numbers from onset (see Table 2). As convection is made up of very small scales at $E = 2 \times 10^{-6}$ and these Ra , the contour plots of the radial velocity in Figs. 5 and 6 are truncated to spherical harmonic degree $l = 32$ for clear visualization of the coherent downwellings, except in Fig. 5(d) where the velocity is computed over the whole range of l . The simulation at $Ra = 10^8$ ($\approx 16.5Ra_c$) shows an isolated downwelling beneath the Atlantic and much weaker convection in the Eastern hemisphere (Figs. 5(a) and 6(a) & (c)). The lowest Rayleigh number at which a similar state of convection occurs in the experiment is $Ra \approx 3.5 \times 10^8$. As Ra is increased to 8×10^8 ($\approx 132Ra_c$), the structure of the flow (Fig. 5(b)) is similar to that in the experiment at $Ra = 8.92 \times 10^8$, with a coherent downwelling beneath the Atlantic and weaker convection beneath Asia (see Fig. 3(c) & 4(a)). The simulation at $Ra = 1.5 \times 10^9$ ($\approx 248Ra_c$) shows the appearance of a coherent downwelling beneath Asia and the break-up of coherent convection into a cluster of rolls beneath the Atlantic (Figs. 5(c); 6(b) & (d)). The cylindrical surface plot of the velocity in Fig. 6(b) reveals the strongly columnar structure of the downwelling, consistent with approximate geostrophy. The lowest Rayleigh number at which this state of convection occurs in the experiment is $Ra \approx 1.7 \times 10^9$ (see Figs. 3(d) & 4(b)). The fine scales of convection in the spherical shell model (Fig. 5(d)) are, however, not present in the experiment. The simulation at $Ra = 2.5 \times 10^9$ (Fig. 5(e)) shows essentially the same flow structure as that at $Ra = 1.5 \times 10^9$, which indicates that the isolated downwelling beneath Asia is a robust feature in strongly driven convection with large lateral variations.

The simulation at $Ra = 6 \times 10^9$ ($\approx 992Ra_c$) shows no preferred longitudinal orientation of convection, which indicates that the radial buoyancy has overcome the influence of the lateral variation in heat flux (Fig. 5(f) & Fig. S1(b) in Supplementary Material). The equivalent experimental state shown in Fig. 3(f) also indicated homogenization of convection. Given that the onset Rayleigh number

is only weakly dependent on q^* for $q^* > 2$, it seems unlikely that strong stratification, produced by much higher values of q^* , would displace the regime of inhomogeneous convection to higher Ra . A high q^* necessitates low E to retain approximate geostrophy of the convection; at this time, laboratory experiments have a clear advantage over numerical simulations in exploring this parameter regime.

The values of the local buoyancy parameter R^* for the Eastern and Western hemispheres in the simulations are given in Table 2. Here, Ra_ℓ and $Ra_{c,\ell}$ are based on the mean equatorial heat flux in the respective hemispheres. As in the experiments, the values of R^* at which a coherent downwelling exists in the East and West are comparable. If $R^* \approx 120$ is taken as the upper bound for the existence of the downwelling in either hemisphere, then simulations in the range $1.15 \times 10^9 < Ra < 3.5 \times 10^9$ would produce inhomogeneous convection that likely results in mobile magnetic flux beneath Canada and quasi-stationary magnetic flux beneath Siberia. Notably, this range of Ra overlaps with that obtained for coherent Siberian convection in the laboratory experiments. While the value of R^* determines the occurrence of the coherent downwelling in simulations (or experiments), the value of Ra enables the comparison of the regimes of coherent convection in the experiments and simulations.

Since the component of gravity perpendicular to the rotation axis makes the dominant contribution to buoyancy (Busse and Carrigan, 1976) and the heat flux variation on the Earth's CMB is approximately symmetric about the equator (Masters et al., 2000), the azimuthal variation of the equatorial CMB heat flux should dominantly influence the structure of core convection (Sahoo and Sreenivasan, 2019). In strongly driven regimes, the annulus experiment without sloping end walls simulates the interaction between the lateral heterogeneity and gravity at the equator rather well. This would explain why the respective values of Ra that produce similar patterns of convection in the experiment and the spherical shell model do not differ much. In the regime close to onset of

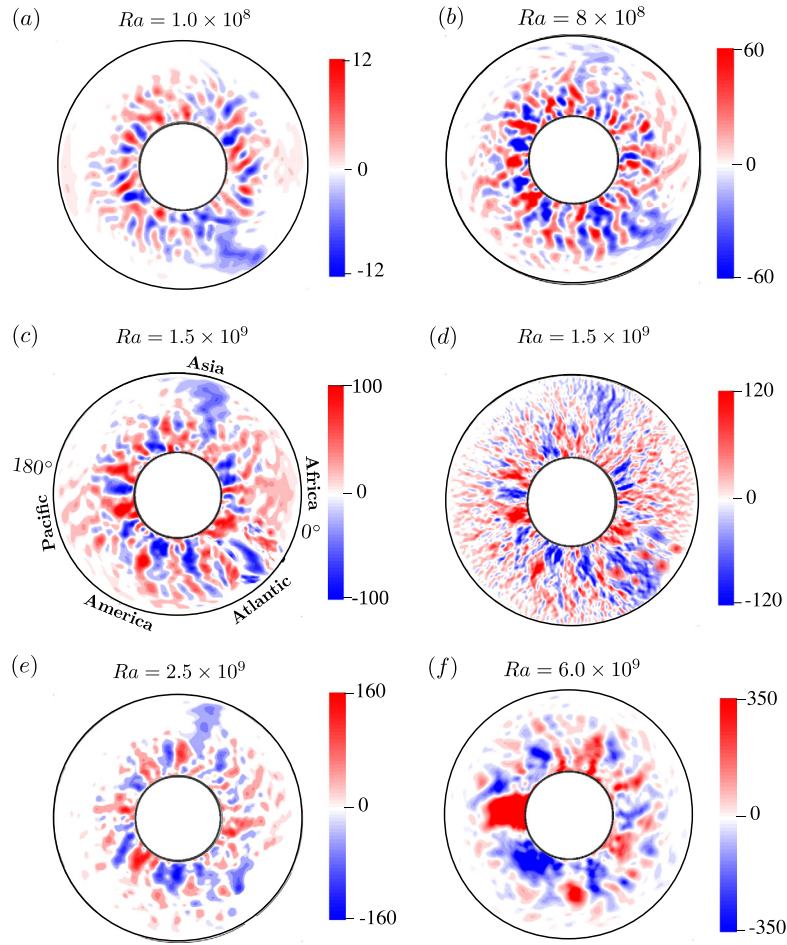


Fig. 5. Equatorial section plots of the radial velocity averaged over ≈ 150 turnover times in the numerical simulations of spherical shell convection. The velocity is truncated to spherical harmonic degree $l = 32$, except in (d), where it is computed over the whole range of l . The Rayleigh number Ra is given above each panel. The fixed parameters are $E = 2 \times 10^{-6}$, $Pr = 1$ and $q^* = 4$.

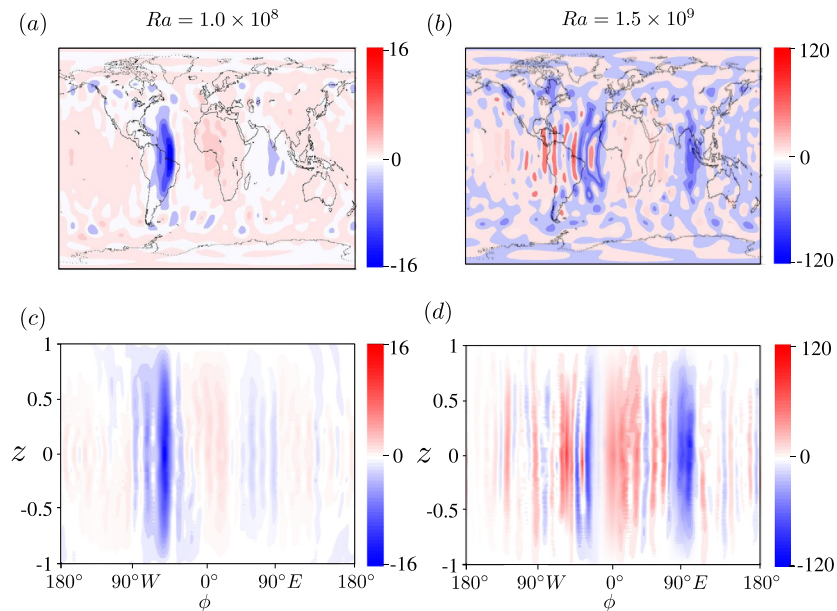


Fig. 6. Plots of the time-averaged radial velocity in the numerical simulations of spherical shell convection. (a) & (b): Velocity on a spherical surface of radius $r = 0.8r_0$. (c) & (d): Velocity on a cylindrical surface of radius $s = 0.72r_0$. The plots are truncated to spherical harmonic degree $l = 32$. The fixed parameters in the simulations are $E = 2 \times 10^{-6}$, $Pr = 1$ and $q^* = 4$.

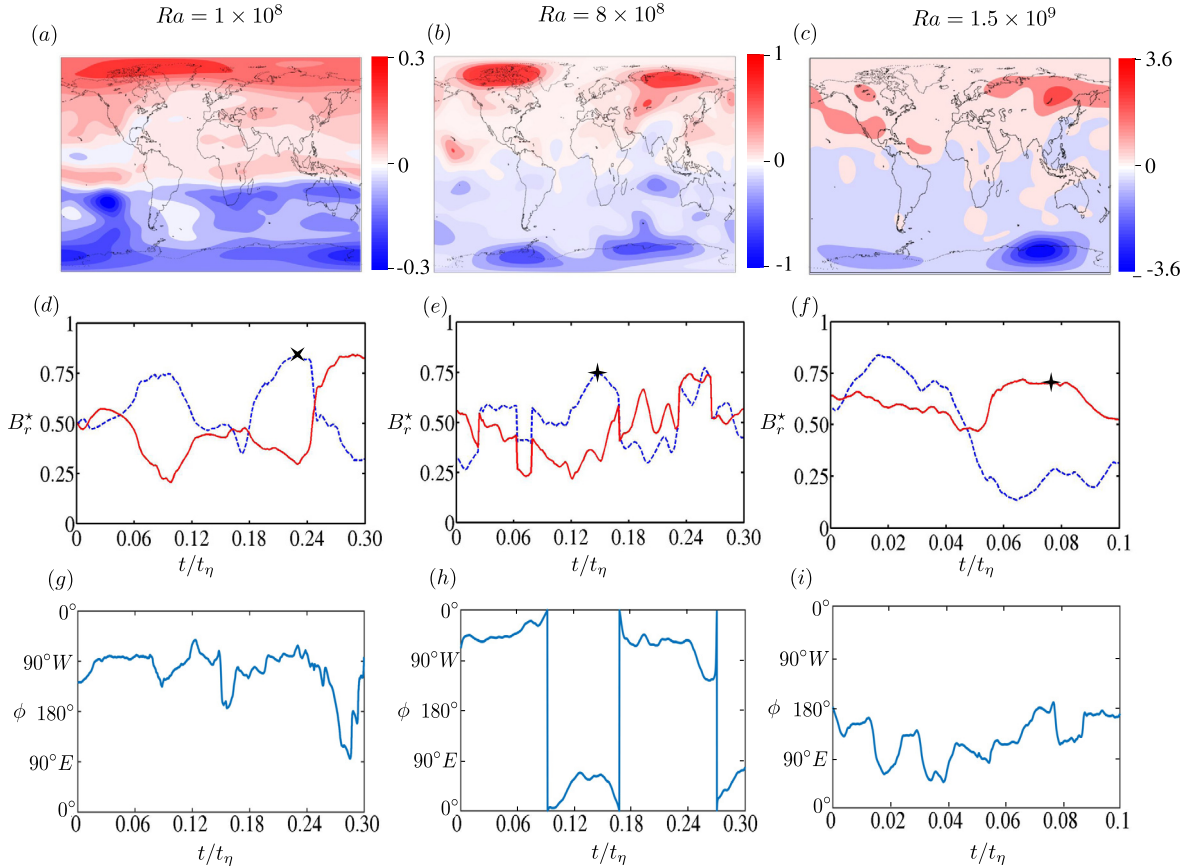


Fig. 7. (a)–(c): Contour plots of the radial magnetic field at the outer boundary truncated to spherical harmonic degree $l = 14$ in the nonlinear dynamo simulations at $E = 2 \times 10^{-6}$, $Pr = Pm = 1$ and three Rayleigh numbers. The plots are averaged over ≈ 150 turnover times. (d)–(f): Evolution of the normalized radial field in the Northern hemisphere, defined by equation (3), with the North-West average shown in blue and the North-East average in red. The stars denote the times at which the radial field is shown in the snapshots given in Fig. S3, Supplementary Material. (g)–(i): Time series of the tilted dipole variation. The overall ranges of the variations are (g) 85.4°N , 85°W – 131°W , (h) 83.1°N , 45°W – 57°E and (i) 81.3°N , 63°E – 172°E .

convection, however, the flow is influenced by geometry as well as the basic state temperature profile. Therefore, a comparison of Ra in the annulus experiment and the spherical model would not be sound near onset.

3.3. Spherical shell dynamo simulations

The dynamo simulations use the same parameters as those in the pure convection runs, with the magnetic Prandtl number $Pm = 1$. The criterion for an Earth-like dynamo, based on the value of Rm (Fig. 7 in Christensen et al., 2010), is satisfied by the runs at $Ra \geq 3 \times 10^8$ in Table 2. While the backreaction of the magnetic field on the convection is not the focus of this paper, we draw the reader's attention to the comparison of the equatorial radial velocity in the convection and dynamo simulations at $Ra = 1.5 \times 10^9$ ($\approx 248Ra_c$). (Fig. S2, Supplementary Material). The Lorentz force preferentially extracts energy from the small-scale flow to feed the magnetic field, so that the clustered convection beneath the Atlantic is considerably weakened. Consequently, the east–west dichotomy of the flow is more pronounced in the dynamo than in pure convection.

The structure of the magnetic field that may result from the convection patterns in Fig. 5 is now examined. Fig. 7(a)–(c) shows the time-averaged radial magnetic field on the outer boundary at progressively increasing strength of convection. Snapshots of the radial field for these cases are presented in Fig. S3 (Supplementary Material). The field is truncated to spherical harmonic degree $l = 14$, as is often done for the observed field (Gubbins et al., 2007;

Olsen et al., 2014). For $Ra = 10^8$, the field is seen to drift systematically westward while being localized for long periods under the Canadian longitude where an isolated weak downwelling is present (Fig. 6(a)). The high-latitude magnetic flux lobes are therefore better visualized in a snapshot (Fig. S3(a), Supplementary Material) than in the time average (Fig. 7(a)). For $Ra = 8 \times 10^8$, the westward drift of the high-latitude field is relatively small, so the four flux lobes show up in the time average (Fig. 7(b)). The Canadian and Siberian pair of lobes are of comparable strength, although the Canadian pair appears slightly stronger. For $Ra = 1.5 \times 10^9$, the Siberian pair of lobes is much stronger (Fig. 7(c)), owing to the strong downwelling beneath Asia and broken convection beneath America (Fig. 6(b) & (d)). In short, the switch of the downwelling from the West to the East is reflected in the West-to-East switch of the dominant pair of magnetic flux lobes.

Since the time variations of the field in the Canadian and Siberian regions are of some historical interest, we look at the time evolution of a normalized radial magnetic field in the Northern hemisphere, defined by

$$B_r^* = \frac{\overline{B_r} - B_r^{\min}}{B_r^{\max} - B_r^{\min}}, \quad (3)$$

where $\overline{B_r}$ is evaluated as surface averages over the North-West ($0^\circ < \theta < 90^\circ\text{N}$, $0^\circ < \phi < 180^\circ\text{W}$) and North-East ($0^\circ < \theta < 90^\circ\text{N}$, $0^\circ < \phi < 180^\circ\text{E}$) sectors, and the maximum and minimum values are measured in the same sectors. At relatively low Rayleigh number, the flow beneath the Siberian region is weak, which in general gives rise to a weaker radial magnetic field compared

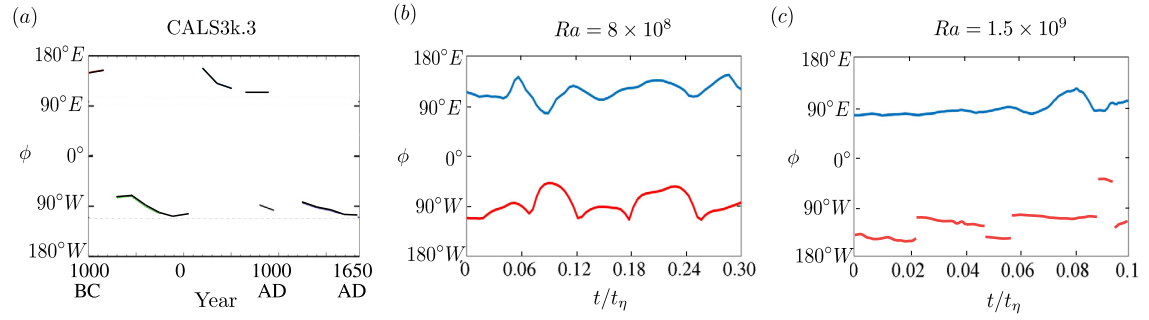


Fig. 8. Time series of the longitude of the peak value of the intense patches in the northern hemisphere. (a) CALS3k.3 field model. (b, c): Numerical dynamo simulations at the Rayleigh numbers (Ra) indicated.

with the Canadian region where an isolated downwelling exists (Fig. 7(d)). At the intermediate Rayleigh number $Ra = 8 \times 10^8$, the flow beneath Canada remains coherent while that beneath Siberia has gained in strength, resulting in average fluxes that are comparable in strength in the North-West and North-East. The flux in the North-West occasionally dominates, as in Fig. 7(b) and (e). At $Ra = 1.5 \times 10^9$, the coherent downwelling that forms beneath Siberia ensures a strong average flux in the North-East compared with the North-West (Fig. 7(f)) where the convection has broken up into a cluster of rolls. The normalized radial field variation in the Southern hemisphere follows a similar trend to that in Fig. 7(d)–(f).

The video `Br_sib.avi` that accompanies this paper shows the radial magnetic field at the outer boundary in the dynamo simulation at $Ra = 1.5 \times 10^9$, $E = 2 \times 10^{-6}$, $Pr = 1$ and $q^* = 4$. The dominance of the Siberian pair of flux lobes over the Canadian pair in a strongly driven regime is evident from this video.

The colatitude θ and longitude ϕ of the dipole field at the upper boundary (CMB) are given by

$$\cos \theta = g_1^0 / |\vec{m}|; \quad \vec{m} = (g_1^0, g_1^1, h_1^1), \quad (4)$$

$$\tan \phi = h_1^1 / g_1^1, \quad (5)$$

where the spherical harmonic dipole coefficients g_1^0 , g_1^1 and h_1^1 are related to the poloidal part of the magnetic field (e.g. Sreenivasan et al., 2014). The time series of the tilted dipole variation for the three dynamo simulations are given in Fig. 7(g)–(i). In these simulations, the magnetic North pole is not far from the geographic North while the longitude shows considerable variation. For $Ra = 10^8$, the dipole variation is mostly confined to the Western hemisphere (Fig. 7(g)), indicating the dominance of the Canadian pair of flux lobes. For $Ra = 8 \times 10^8$, the dipole axis is seen to oscillate between 45°W – 57°E through the Greenwich meridian (Fig. 7(h)), showing approximate parity between the Canadian and Siberian pair. For $Ra = 1.5 \times 10^9$, a large variation confined to the Eastern hemisphere is noted (Fig. 7(i)), showing the dominance of the Siberian pair. Therefore, in the regime of strongly driven convection ($Ra > 8 \times 10^8$) and large q^* , one would anticipate a West-to-East migration of the magnetic North pole. The pole drifted eastward at the rate 50 – 60 km yr^{-1} at the beginning of this century (see Olsen and Manda, 2007; Korte and Manda, 2008). Variations in the polar drift rate may be correlated to changes in the Rayleigh number, all other parameters remaining the same.

The longitudinal locations of the peak value of localized flux patches in both Northern and Southern hemispheres are shown in Fig. 8. The east–west variability of the field in the dynamo simulation is compared with that from the archeomagnetic field model CALS3k.3 (Amit et al., 2011), where the Northern flux patches move approximately within longitudes 105°E – 150°E in the Eastern hemisphere and within longitudes 75°W – 120°W in the Western hemisphere. In the dynamo at $Ra = 8 \times 10^8$, the flux patches are

mostly localized within longitudes 85°E – 135°E and 65°W – 110°W . While there is no systematic westward drift for the high latitude flux patches, the equatorial flux patches seem to drift westward at a reduced rate compared with the dynamo run at $Ra = 10^8$. For $Ra = 1.5 \times 10^9$, the broken patches in the Western hemisphere have a higher east–west variability than the concentrated patches in the Eastern hemisphere. Although these broken patches disappear and then reappear at different locations (Fig. 8(c)), their variability can be estimated to lie within longitudes 105°W – 153°W . The peaks of the concentrated flux patches in the Eastern hemisphere lie within longitudes 80°E – 130°E . In addition, the westward drift rate of equatorial flux patches is further reduced compared with that in the run at $Ra = 8 \times 10^8$. Overall, the longitudinal variability of the high-latitude flux lobes in our dynamo simulations at large Ra and q^* is in fair agreement with the historical data.

4. Concluding remarks

The lateral variation in heat flux across the Earth's CMB can be at least twice the mean heat flux (Nakagawa and Tackley, 2008; Olson et al., 2015). Spherical shell simulations of the core that use moderate-to-large variations of the CMB heat flux derived from present day seismic tomography do not reveal any substantial east–west dichotomy either in convection (Mound and Davies, 2017; Mound et al., 2019) or in the magnetic field (Olson and Christensen, 2002; Gubbins et al., 2007; Takahashi et al., 2008; Amit et al., 2015; Terra-Nova et al., 2019). The idea that the pattern of inhomogeneous convection in the core may be substantially different from the simplified two-fold ($m = 2$) pattern rests on two factors: First, the onset of convection at the equator beneath Asia occurs at a higher Rayleigh number than that beneath America, so the patterns of convection in the West are replicated in the East at higher Rayleigh number. Second, approximate geostrophy in the face of large q^* ensures the east–west segregation of columnar convection. As these factors are practically independent of geometry, the annulus experiment provides useful data in strongly driven regimes whose simulation is computationally demanding. The good agreement between the large-scale convection patterns in the experiment and the spherical shell simulation indicates that the effects produced by sloping boundaries – the rotational dependence of the flow length scale and the Rossby wave-like drift of rolls – do not significantly influence the distribution of convection.

A coherent downwelling beneath Siberia, which forms despite the stronger seismic anomaly beneath Canada, would be the likely consequence of a large lower mantle heterogeneity in present day Earth. Given that convection homogenizes in both the annulus experiment and the spherical shell model at comparable Ra ($\sim 6 \times 10^9$) and very different Ra/Ra_c (~ 50 for the annulus and $\sim 10^3$ for the spherical shell), we anticipate that the range of Ra for coherent Siberian convection would persist for lower E . It is ev-

ident that the stable stratification produced beneath Africa and the Pacific in the simulations does not significantly change the range of Ra for coherent Siberian convection from that in the experiments without stratification. This result is adequately explained by the weak dependence of Ra_c on q^* for $q^* > 2$ and $E \sim 10^{-6}$ (Sahoo and Sreenivasan, 2017). As larger lateral variations do not introduce significant changes to the onset, the east–west dichotomy of the convection would be similar, so our simulations at $q^* = 4$ may be considered Earth-like. Our values of Ra that give Earth-like magnetic fields are $\sim 10^3$ times lower than the estimates for the Earth's core using turbulent diffusivities (Gubbins, 2001). Apart from the uncertainties in the diffusivities, the effects of secular cooling of the core and spatially homogeneous core stratification arising from the basic state buoyancy profile (e.g. Lister and Buffett, 1998; Bouffard et al., 2019) may change the estimate of Ra for the core. Consideration of these effects in the simulations with lowering of E to a value for the core given by the turbulent viscosity would result in enhanced values for both Ra_c and Ra . However, we anticipate that the range of $Ra/Ra_c \sim [190, 420]$ – that give Earth-like magnetic fields in our dynamo models – would not change considerably. Notably, this range of Ra/Ra_c does not differ much from the estimate $\sim 10^3$ for non-magnetic compositional convection (Gubbins, 2001). This agreement is consistent with the idea that the value of Ra_c in magnetoconvection with spatially inhomogeneous magnetic fields would not differ much from that in non-magnetic convection (Sreenivasan and Gopinath, 2017).

A related issue is whether the east–west dichotomy in core convection would result in a lateral heterogeneity on the ICB (Bergman, 1997; Deuss, 2014). Spherical simulations that consider secular cooling of the core in the basic state buoyancy profile (Gubbins et al., 2011) as well as laboratory experiments in an annulus (Sahoo and Sreenivasan, 2019) indicate that the heterogeneity at the CMB is amplified at the ICB due to inhomogeneous core convection. That said, recent simulations that consider basal heating in the basic state (Davies and Mound, 2019) suggest that the lower-mantle variations may not propagate to the ICB. This problem needs further analysis with models that consider the combined effects of thermal and compositional buoyancy.

CRedit authorship contribution statement

Swarandeeep Sahoo: Methodology, Investigation, Formal Analysis, Writing; **Binod Sreenivasan:** Conceptualization, Methodology, Investigation, Writing, Funding acquisition.

Declaration of competing interest

The authors declare that they have no known competing financial interests or personal relationships that could have appeared to influence the work reported in this paper.

Acknowledgements

This study was supported by Research Grant no. 5307-1 awarded by the Indo-French Centre for the Promotion of Advanced Research (IFCPAR). B.S. was awarded a SwarnaJayanti Fellowship by the Department of Science and Technology (India) during the early stages of this project. The computations were performed on SahasraT, the supercomputer at IISc Bangalore.

Appendix A. Supplementary material

Supplementary material related to this article can be found online at <https://doi.org/10.1016/j.epsl.2020.116507>.

References

- Ahlers, G., Brown, E., Araujo, F., Funfschilling, D., Grossmann, S., Lohse, D., 2006. Non-Oberbeck-Boussinesq effects in strongly turbulent Rayleigh–Bénard convection. *J. Fluid Mech.* 569, 409–445.
- Amit, H., Deschamps, F., Choblet, G., 2015. Numerical dynamos with outer boundary heat flux inferred from probabilistic tomography – consequences for latitudinal distribution of magnetic flux. *Geophys. J. Int.* 203 (2), 840–855.
- Amit, H., Korte, M., Aubert, J., Constable, C., Hulot, G., 2011. The time-dependence of intense archeomagnetic flux patches. *J. Geophys. Res.* 116, B12106. <https://doi.org/10.1029/2011JB008538>.
- Aubert, J., Amit, H., Hulot, G., Olson, P., 2008. Thermo-chemical wind flows couple Earth's inner core growth to mantle heterogeneity. *Nature* 454, 758–761.
- Aubert, J., Brito, D., Nataf, H.-C., Cardin, P., Masson, J.P., 2001. A systematic experimental study of rapidly rotating spherical convection in water and liquid gallium. *Phys. Earth Planet. Inter.* 128, 51–74.
- Aurnou, J.M., Calkins, M.A., Cheng, J.S., Julien, K., King, E.M., Nieves, D., Soderlund, K.M., Stellmach, S., 2015. Rotating convective turbulence in Earth and planetary cores. *Phys. Earth Planet. Inter.* 246, 52–71.
- Azouni, M.A., Bolton, E.W., Busse, F.H., 1985. Convection driven by centrifugal buoyancy in a rotating annulus. *Geophys. Astrophys. Fluid Dyn.* 34 (1–4), 301–317.
- Bergman, M.I., 1997. Measurements of electric anisotropy due to solidification texturing and the implications for the earth's inner core. *Nature* 389 (6646), 60.
- Bloxham, J., Gubbins, D., 1987. Thermal core-mantle interactions. *Nature* 325, 511–513.
- Bouffard, M., Choblet, G., Labrosse, S., Wicht, J., 2019. Chemical convection and stratification in the Earth's outer core. *Front. Earth Sci.* 7, 99.
- Busse, F.H., Carrigan, C.R., 1974. Convection induced by centrifugal buoyancy. *J. Fluid Mech.* 62 (3), 579–592.
- Busse, F.H., Carrigan, C.R., 1976. Laboratory simulation of thermal convection in rotating planets and stars. *Science* 191, 81–83.
- Cardin, P., Olson, P., 1994. Chaotic thermal convection in a rapidly rotating spherical shell: consequences for flow in the outer core. *Phys. Earth Planet. Inter.* 82, 235–259.
- Carrigan, C.R., Busse, F.H., 1983. An experimental and theoretical investigation of the onset of convection in rotating spherical shells. *J. Fluid Mech.* 126, 287–305.
- Christensen, U., Aubert, J., Hulot, G., 2010. Conditions for Earth-like geodynamo models. *Earth Planet. Sci. Lett.* 296, 487–496.
- Davies, C.J., Mound, J.E., 2019. Mantle-induced temperature anomalies do not reach the inner core boundary. *Geophys. J. Int.* 219 (Supplement_1), S21–S32.
- Deuss, A., 2014. Heterogeneity and anisotropy of Earth's inner core. *Annu. Rev. Earth Planet. Sci.* 42, 103–126.
- Dormy, E., Soward, A.M., Jones, C.A., Jault, D., Cardin, P., 2004. The onset of thermal convection in rotating spherical shells. *J. Fluid Mech.* 501, 43–70.
- Grand, S.P., 2002. Mantle shear-wave tomography and the fate of subducted slabs. *Philos. Trans. R. Soc. Lond. Ser. A, Math. Phys. Sci.* 360 (1800), 2475–2491.
- Gubbins, D., 2001. The Rayleigh number for convection in the Earth's core. *Phys. Earth Planet. Inter.* 128, 3–12.
- Gubbins, D., Kelly, P., 1993. Persistent patterns in the geomagnetic field over the past 2.5 Myr. *Nature* 365 (6449), 829–832.
- Gubbins, D., Sreenivasan, B., Mound, J., Rost, S., 2011. Melting of the Earth's inner core. *Nature* 473, 361–363.
- Gubbins, D., Willis, A.P., Sreenivasan, B., 2007. Correlation of Earth's magnetic field with lower mantle thermal and seismic structure. *Phys. Earth Planet. Inter.* 162, 256–260.
- Hart, J.E., Glatzmaier, G.A., Toomre, J., 1986. Space-laboratory and numerical simulations of thermal convection in a rotating hemispherical shell with radial gravity. *J. Fluid Mech.* 173, 519–544.
- Hoffman, K., Singer, B., Camps, P., Hansen, L.N., Johnson, K., Clipperton, S., Carvalho, C., 2008. Stability of mantle control over dynamo flux since the mid-Cenozoic. *Phys. Earth Planet. Inter.* 169 (1–4), 20–27.
- Jackson, A., Jonkers, A.R.T., Walker, M.R., 2000. Four centuries of geomagnetic secular variation from historical records. *Philos. Trans. R. Soc. Lond. A* 358, 957–990.
- Korte, M., Mandea, M., 2008. Magnetic poles and dipole tilt variation over the past decades to millennia. *Earth Planets Space* 60 (9), 937–948.
- Lister, J.R., Buffett, B.A., 1998. Stratification of the outer core at the core-mantle boundary. *Phys. Earth Planet. Inter.* 105 (1–2), 5–19.
- Masters, G., Johnson, S., Laske, G., Bolton, H., Davies, J., 1996. A shear-velocity model of the mantle. *Philos. Trans. R. Soc. Lond. Ser. A, Math. Phys. Sci.* 354 (1711), 1385–1411.
- Masters, G., Laske, G., Bolton, H., Dziewonski, A., 2000. The relative behavior of shear velocity, bulk sound velocity, and compressional velocity in the mantle: implications for chemical and thermal structure. In: Karato, S., Forte, A.M., Liebermann, R.C., Masters, G., Stixrude, L. (Eds.), *Earth's Deep Interior*. In: AGU Monograph, vol. 117, Washington D.C.
- Mound, J., Davies, C., Rost, S., Aurnou, J., 2019. Regional stratification at the top of Earth's core due to core-mantle boundary heat flux variations. *Nat. Geosci.* 12 (7), 575–580.
- Mound, J.E., Davies, C.J., 2017. Heat transfer in rapidly rotating convection with heterogeneous thermal boundary conditions. *J. Fluid Mech.* 828, 601–629.

- Nakagawa, T., Tackley, P.J., 2008. Lateral variations in CMB heat flux and deep mantle seismic velocity caused by a thermal-chemical-phase boundary layer in 3D spherical convection. *Earth Planet. Sci. Lett.* 271, 348–358.
- Olsen, N., Lühr, H., Finlay, C.C., Sabaka, T.J., Michaelis, I., Rauberg, J., Tøffner-Clausen, L., 2014. The CHAOS-4 geomagnetic field model. *Geophys. J. Int.* 197 (2), 815–827.
- Olsen, N., Manda, M., 2007. Will the magnetic North Pole move to Siberia?. *Eos* 88 (29), 293.
- Olson, P., 2016. Mantle control of the geodynamo: consequences of top-down regulation. *Geochem. Geophys. Geosyst.* 17 (5), 1935–1956.
- Olson, P., Christensen, U., 2002. The time averaged magnetic field in numerical dynamos with nonuniform boundary heat flow. *Geophys. J. Int.* 151, 809–823.
- Olson, P., Deguen, R., Rudolph, M., Zhong, S., 2015. Core evolution driven by mantle global circulation. *Phys. Earth Planet. Inter.* 243, 44–55.
- Sahoo, S., Sreenivasan, B., 2017. On the effect of laterally varying boundary heat flux on rapidly rotating spherical shell convection. *Phys. Fluids* 29 (8), 086602.
- Sahoo, S., Sreenivasan, B., 2019. Convection in a rapidly rotating cylindrical annulus with laterally varying boundary heat flux. *J. Fluid Mech.* <https://doi.org/10.1017/jfm.2019.847>.
- Sreenivasan, B., 2009. On dynamo action produced by boundary thermal coupling. *Phys. Earth Planet. Inter.* 177, 130–138.
- Sreenivasan, B., Gopinath, V., 2017. Confinement of rotating convection by a laterally varying magnetic field. *J. Fluid Mech.* 822, 590–616.
- Sreenivasan, B., Sahoo, S., Dhama, G., 2014. The role of buoyancy in polarity reversals of the geodynamo. *Geophys. J. Int.* 199 (3), 1698–1708.
- Sumita, I., Olson, P., 1999. A laboratory model for convection in earth's core driven by a thermally heterogeneous mantle. *Science* 286 (5444), 1547–1549.
- Sumita, I., Olson, P., 2002. Rotating thermal convection experiments in a hemispherical shell with heterogeneous boundary heat flux: implications for the Earth's core. *J. Geophys. Res., Solid Earth* 107. B8.
- Takahashi, F., Tsunakawa, H., Matsushima, M., Mochizuki, N., Honkura, Y., 2008. Effects of thermally heterogeneous structure in the lowermost mantle on the geomagnetic field strength. *Earth Planet. Sci. Lett.* 272 (3–4), 738–746.
- Terra-Nova, F., Amit, H., Choblet, G., 2019. Preferred locations of weak surface field in numerical dynamos with heterogeneous core–mantle boundary heat flux: consequences for the South Atlantic Anomaly. *Geophys. J. Int.* 217 (2), 1179–1199.
- Van der Hilst, R.D., Widiyantoro, S., Engdahl, E., 1997. Evidence for deep mantle circulation from global tomography. *Nature* 386 (6625), 578–584.
- Willis, A.P., Sreenivasan, B., Gubbins, D., 2007. Thermal core-mantle interaction: exploring regimes for 'locked' dynamo action. *Phys. Earth Planet. Inter.* 165, 83–92.
- Zhang, K., Gubbins, D., 1996. Convection in a rotating spherical fluid shell with an inhomogeneous temperature boundary condition at finite Prandtl number. *Phys. Fluids* 8 (5), 1141–1148.